Article

Dual Sensitization via Electron and Energy Harvesting in a Nanohybrid for Improvement of Therapeutic Efficacy

Arpan Bera, Md. Nur Hasan, Arka Chatterjee, Dipanjan Mukherjee, and Samir Kumar Pal*

Cite This: *ACS Phys. Chem Au* 2022, 2, 171−178

Read Online

ACCESS | Metrics & More | Article Recommendations | Supporting Information

ABSTRACT: We demonstrate experimental evidence of the effect of surface plasmon resonance of noble metal nanoparticles (NPs) on the activity of a well-known biomedicinal drug in the proximity of a semiconductor having a wide band gap for enhanced photodynamic therapy (PDT) efficacy. We have chosen riboflavin (Rf) (or vitamin B$_2$) as a model photosensitizer, attached with ZnO NPs and further attached with gold (Au) NP-decorated ZnO to increase the efficiency. The synthesized nanohybrids are characterized with the help of different microscopic, optical spectroscopic, and density functional theory (DFT)-based techniques. The DFT and time-dependent DFT-based calculations validate the experimental findings. A detailed ultrafast spectroscopic study has been carried out further to study the excited-state charge dynamics in the

interface of the nanohybrids. The occurrence of a Förster resonance energy transfer (FRET) between Rf and Au has been found to be the key reason for the increased efficiency in the Rf−ZnO−Au nanohybrid over the Rf−ZnO one. The dipolar coupling between Au and Rf in the Rf−ZnO−Au nanohybrid further facilitates the generation of reactive oxygen species (ROS) in comparison to Rf−ZnO under blue-light irradiation. The greater efficiency in ROS generation by the Rf−ZnO−Au nanohybrid has been utilized for antimicrobial action against methicillin-resistant *S. aureus* (MRSA). Overall, the present study highlights the dual sensitization for achieving enhanced electron injection efficiency in the Rf−ZnO−Au nanohybrid in order to use it as an antibacterial agent that could be translated in PDT.

KEYWORDS: *Rf−ZnO nanohybrid, Rf-ZnO-Au nanohybrid, ultrafast spectroscopy, ROS, antibacterial activity*
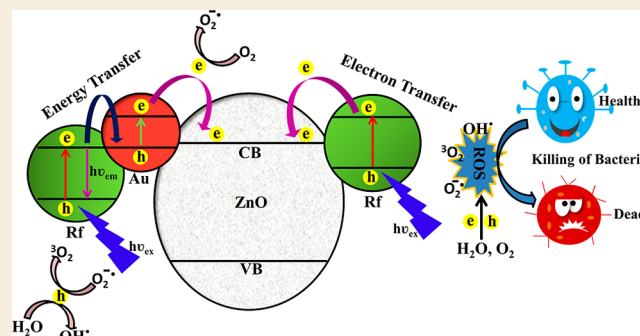
1. INTRODUCTION

Photodynamic therapy (PDT) is a revolutionary most exciting therapy strategy that involves non-invasive treatment of cancers of various types and locations.[1−4] It depends on the application of a photosensitizer (PS), which is intensely assembled in pathological tissues. The PS molecules generate reactive oxygen species (ROS) upon excitation at a particular wavelength which involves the selective destruction of infected cells.[5] Over the past 5 decades, riboflavin (Rf) or vitamin B$_2$ has been used as a potential photosensitizer because of its tremendous ROS generation ability under visible light irradiation.[6,7] It is a water-soluble essential micronutrient and is substantially available in dietary products of both vegetable and animal origin.[8−10]

The effectiveness of PDT depends on the photoexcitation of the PS assembled at the target sites as well as its pharmacokinetic properties to achieve the desired biological response. However, the conventional therapeutic agents have some limitations such as poor solubility, short circulation time, high immunogenicity, and non-specific distribution throughout the body, which lead to the induction of various side effects in normal tissues.[11,12] Nanomaterials as drug carriers can

overcome these limitations as they exhibit upgraded pharmacokinetics and biodistribution of drugs, and their accumulation at the targeted site reduces toxicity.[13] Also, the solubility of hydrophobic drugs increases upon their formulation as nanoconjugates.[14] Moreover, sensitization of drugs by inorganic NPs through formulation of a nanohybrid is key for the enhancement of drug activity.[15] In recent years, a variety of nanohybrids have been used to deliver drugs and biomolecules to achieve satisfying therapeutic effects.[16−18] Among all, ZnO-based nanohybrids are most promising in terms of modulation of drug activity, disease site-specific targeted delivery, and less toxicity.[19]

Utilization of dual sensitization can be very useful in order to get more efficiency in PDT. This novel approach is based on the Förster resonance energy transfer (FRET) between

covalently linked donor molecules to the acceptor, attached to the surface of the semiconductor which has been previously used to enhance the efficiency in dye-sensitized solar cells.[20,21] In recent times, a few groups have reported dual-sensitized nanohybrids consisting of quantum dots and upconversion nanomaterials.[22−26] All the earlier reported nanohybrids are not only toxic but also require complicated and expensive methods for their synthesis. However, the implementation of this kind of system in PDT is not highlighted in the contemporary literature. In this regard, development of an organic/inorganic nanohybrid system using plasmonic NPs could be a better solution for the enhanced efficacy of PDT and thus is one of the main motives of the present work.

Herein, we have selected Rf as a model photosensitizer, which is attached with ZnO NPs and further attached with Au-decorated ZnO. We have specifically chosen Au as the noble metal because of its greater biocompatibility than other noble metals and the ease of synthesis.[27] The sizes of the NPs and decoration of Au on the ZnO surface are confirmed by electron microscopic techniques. The attachment of Rf has been investigated by optical spectroscopic and DFT-based methods. The picosecond-resolved fluorescence study explores the excited-state photoelectron-transfer process from Rf to ZnO and FRET from RF to Au in Rf−ZnO−Au nanohybrids, which has been confirmed by the fluorescence transient of the Rf−Al$_2$O$_3$−Au nanohybrid. The presence of Au influences huge charge separation in the Rf−ZnO−Au nanohybrid upon blue-light irradiation which leads to greater production of ROS upon blue-light irradiation. The Rf−ZnO−Au nanohybrids show enhanced antibacterial activity in a dose-dependent manner against MRSA due to photoinduced ROS. In short, the present study demonstrates the dual sensitization of Rf for enhanced ROS generation for potential antibacterial activity that could be effective for PDT.

2. MATERIALS AND METHODS

The chemicals of analytical grade were used without further modification. ZnO NPs (size <50 nm), Al$_2$O$_3$ NPs (size <50 nm), Rf, and chloroauric acid (HAuCl$_4$·H$_2$O) were purchased from Sigma-Aldrich. Ethanol was purchased from Merck, and Millipore water was used for aqueous solutions. The DCFH-DA (2,7-dichlorodihydro-fluorescein diacetate) probe was purchased from Calbiochem for the DCFH oxidation assay. In order to investigate the antibacterial activity of the Rf−ZnO−Au nanohybrid, Luria-Bertani broth (LB) and LB top agar from HIMEDIA were used as media.

2.1. Synthesis of the Rf−ZnO Nanohybrid

The Rf−ZnO nanohybrid was synthesized by addition of ZnO NPs (10 mg) to 10 mL of Rf solution (0.5 mM solution in ethanol) under magnetic stirring at room temperature for 12 h. After that, the solution was centrifuged for 30 min and washed with ethanol four times to wash out free dyes. The nanohybrid was then dried in an oven for 4 h at 70 °C.

2.2. Synthesis of the Au−ZnO Nanohybrid

12 mg of ZnO NPs was slowly added to 5 mL of 1 mM chloroauric acid (HAuCl$_4$·H$_2$O) aqueous solution under continuous stirring for 15 min at room temperature. Then, an aqueous solution of 5 mM sodium borohydride (NaBH$_4$) was added dropwise to the solution for the reduction of gold chloride to Au NPs. Immediately, the solution turned red from pale yellow, indicating the decoration of the Au NPs on the surface of ZnO NP NPs.

2.3. Synthesis of the Rf−ZnO−Au Nanohybrid

The Rf−ZnO−Au nanohybrid was synthesized upon addition of 10 mg of the Au−ZnO nanohybrid to 10 mL of Rf solution (0.5 mM solution in ethanol) at room temperature under continuous stirring

for 14 h. The solution was then centrifuged for 20 min and washed with ethanol four times to remove any free Rf. The synthesized Rf−ZnO−Au nanohybrid was then dried in the oven for 4 h at 70 °C.

2.4. Synthesis of Rf−Al$_2$O$_3$ and Rf−Al$_2$O$_3$−Au Nanohybrids

The Rf−Al$_2$O$_3$ nanohybrid was synthesized upon addition of 10 mg of Al$_2$O$_3$ NPs to 10 mL of Rf solution (0.5 mM solution in ethanol) under magnetic stirring at room temperature for 12 h. After that, the solution was centrifuged for 30 min and washed with ethanol and double-distilled water four times to wash out free dyes. The nanohybrid was then dried in the oven for 4 h at 80 °C. The Al$_2$O$_3$−Au nanohybrid was synthesized by following the synthesis procedure of the Au−ZnO nanohybrid. The Rf−Al$_2$O$_3$−Au nano-hybrid was synthesized by adding 10 mg of the synthesized Al$_2$O$_3$−Rf nanohybrid to the Rf solution in ethanol (0.5 mM), followed by continuous stirring at room temperature for 14 h. The solution was then centrifuged for 30 min, and the prepared Rf−Al$_2$O$_3$−Au nanohybrid was dried in the oven for 4 h at 70 °C.

2.5. Characterization Techniques

In order to prepare the samples for transmission electron microscopy (TEM) analysis, diluted solutions of Au−ZnO in ethanol were spread over a carbon-coated copper grid. In order to record X-ray diffraction (XRD) patterns, the samples were measured using a PAN analytical XPERTPRO diffractometer equipped with Cu Kα radiation (at 40 mA and 40 kV) at a rate of 0.02° S^{-1} in the 2θ range from 30 to 70°. A Shimadzu spectrophotometer (UV-2600) and a HORIBA Fluorolog were used to measure absorption and steady-state emissions, respectively. To measure time-resolved photolumines-cence, a time-correlated single-photon counting setup from Edinburgh Instruments was used. The measured IRF (instrument response function) was 80 ps. The nonlinear least-squares procedure was used to fit the fluorescence transients.[28] The Förster distance (R_0) is determined by

$$R_0 = 0.211 \times [\kappa^2 \eta^{-4} Q_D J]^{1/6} \tag{1}$$

After getting the value of R_0, the distance (r) between the donor and the acceptor was calculated using the following equation

$$r^6 = (1 - E)/E \tag{2}$$

where E is the efficiency of energy transfer.

2.6. Measurement of ROS

DCFH was prepared by the de-esterification reaction of DCFH-DA.[29] Rf (1.2 μM), the Rf−ZnO nanohybrid (the concentration of Rf in the nanohybrid is 1.2 μM), the Rf−ZnO−Au nanohybrid (the concentration of Rf is 1.2 μM), the Rf−Al$_2$O$_3$ nanohybrid (the concentration of Rf in the nanohybrid is 1.2 μM), the Rf−Al$_2$O$_3$−Au nanohybrid (the concentration of Rf in the nanohybrid is 1.2 μM), and Au−ZnO (the concentration of Au−ZnO is the same as the concentration of Au−ZnO in Rf−ZnO−Au) were used for ROS measurements.

2.7. Bacterial Strain and Culture Conditions

The strain of methicillin-resistant *S. aureus* (MRSA) was used for the bacteriological assay. The cells were incubated with 0.20 mg/mL Rf−ZnO−Au nanohybrid or Rf−ZnO nanohybrid, and others as the control (the concentration of Rf was used on the basis of Rf loading on the ZnO surface, and the concentrations of ZnO and Au−ZnO were equivalent to the concentration of the Rf−ZnO−Au nano-hybrid) for 3 h. The experiments were performed in the absence as well as in the presence of blue light (λ_{max} = 409 nm) for 30 min. The colony forming units (CFU) of *S. aureus* were counted to quantify the antibacterial activity.

3. COMPUTATIONAL METHODS

The structure of Rf vitamin was obtained from PubChem (CID 493570). The DFT and TD-DFT calculations were performed in Gaussian 16 software. Geometric optimization of the pristine Zn$_{12}$O$_{12}$ nanocage was performed at the level of DFT using the B3LYP[30−32]

exchange correlation functional and the 6-311++g(d,p)[33] basis set. It is composed of eight $(ZnO)_3$ and six $(ZnO)_2$ rings forming a cluster.[34,35] To prepare the Au-doped $Zn_{12}O_{12}$ structure of NPs, several doping configurations were optimized with the B3LYP/6-311++G(d,p)-SDD-based method,[36] and further calculations were carried out with the most favorable structure. The band-gap energies (E_g) were calculated from the energy of the lowest unoccupied molecular orbital (E_{LUMO}) and the energy of the highest occupied molecular orbital (E_{HOMO}) in the following form

$$E_g = E_{LUMO} - E_{HOMO} \tag{3}$$

Density of states (DOS) for all the studied structures was plotted by using the GaussSum 2.1.4 program.[37]

4. RESULTS AND DISCUSSION

Figure 1a,b shows the HRTEM image of Au-decorated ZnO NPs. It depicts Au NPs that are uniformly decorated on the
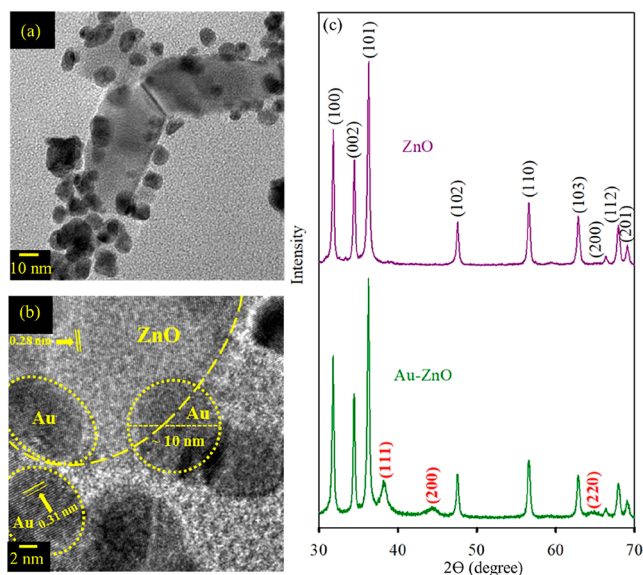

Figure 1. (a) TEM image of Au−ZnO. (b) HRTEM image of Au−ZnO. (c) Powder XRD pattern of ZnO (violet) and Au−ZnO (green).

surface of ZnO, and the average diameter of Au NPs is found to be ~10 nm. The interplanar distance of the lattice fringes of ZnO NPs is measured to be 0.28 nm, which corresponds to the (100) crystal planes. Whereas, an interplanar distance of 0.31 nm for the Au NPs signifies the (222) crystal planes.[28,38] The low-magnification TEM images of Au−ZnO show the uniform decoration of Au on the surface of ZnO (Figure S1a−c). The size distribution of Au nanoparticles (NPs) on the surface of ZnO has been calculated (Figure S1d). The average size of Au NPs is found to be ~9 nm. We have investigated the EDAX spectra of at least 20 NPs and found them to be consistent. The compositional analysis of Au−ZnO is obtained from EDAX, as shown in Figure S2 and tabulated in Table S1. The atomic percentage of Au is found to be 6.85. Figure 1c displays characteristic XRD patterns of ZnO and Au−ZnO hybrids. The diffraction pattern of ZnO NPs suggests a hexagonal wurtzite structure.[39] The decoration of Au NPs on the surface of ZnO NPs could not change the position of the diffraction peaks of ZnO, which indicates that the surface of ZnO remains intact upon Au decoration. However, some additional characteristic peaks of Au NPs appear in the XRD pattern of the Au−ZnO nanohybrids. The positions $(2\theta$ value) of the

diffraction peaks of Au NPs are observed to be at 38.13, 44.28, and 64.55°, which signify the (111), (200), and (220) crystal planes, respectively.[40]

The absorption spectra (Figure 2a) of Rf in ethanol exhibit two characteristic peaks at 351 and 445 nm. In the case of Rf−
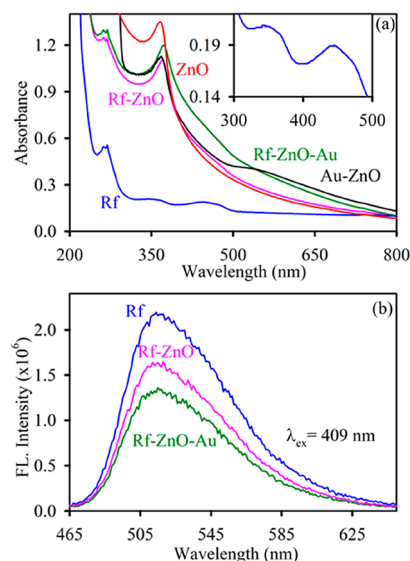

Figure 2. (a) UV−vis absorption spectra of Rf (blue), Rf−ZnO (pink), ZnO (red), Au−ZnO (black), and Rf−ZnO−Au (green) in ethanol. The inset shows enlarge absorption spectra of Rf in ethanol, (c) room-temperature emission spectra of Rf (blue), Rf−ZnO (pink), and Rf−ZnO−Au (green) in ethanol.

ZnO and Rf−ZnO−Au, the change in the absorbance peak at 445 nm indicates the complex formation between Rf and the surfaces of both ZnO and Au−ZnO, as shown in Figure 2a.[17,28] The absorption spectra of Au−ZnO possess two characteristic peaks of Au and ZnO at 536 and 369 nm, respectively. No distinct peak of Rf is observed in both nanohybrids due to a very low concentration of Rf and significant scattering of the NPs. However, the characteristic peak of ZnO is visible for both nanohybrids. However, the attachment of Rf is concluded from the steady-state emission spectrum. It shows a sharp emission peak at 520 nm upon excitation at 409 nm in ethanol. In the case of Rf−ZnO and Rf−ZnO−Au, the characteristic peak of Rf is observed along with significant quenching in emission intensity, as depicted in Figure 2b. The emission quenching for both nanohybrids signifies the existence of the excited-state non-irradiative process.

Further, the DFT- and TD-DFT-based computational calculations are performed to understand the electronic structures. Computational investigations are particularly useful for understanding trends observed in the properties of molecular materials. The structure of Rf is optimized by the DFT/B3LYP method, as shown in the inset of Figure S2a. The UV−vis absorption spectra are calculated using the most stable structure of Rf by the TD-DFT/B3LYP-based method, as depicted in Figure S3a, which well matches with experimental absorption. Figure S3b depicts the calculated emission spectra of Rf. The calculated emission peak is well consistent with the experimental findings. The TDOS of Rf is calculated using the DFT/B3LYP exchange correlation functional method and plotted in GaussSum 2.1.4 software, as shown in Figure S4a. It is composed of the valence band (VB) and conduction band
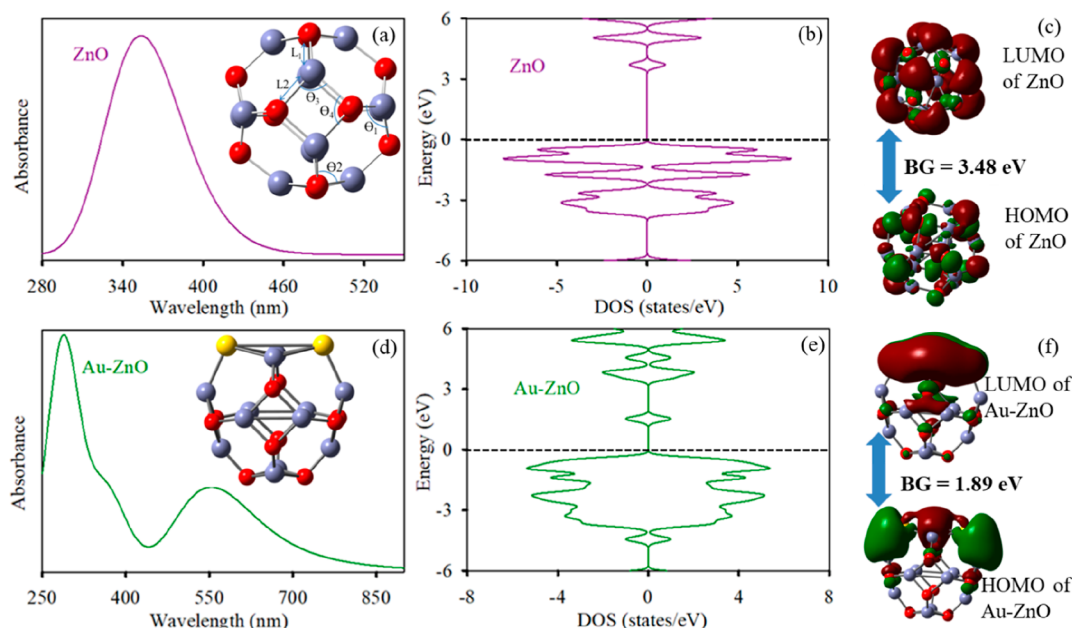
Figure 3. (a) Theoretical UV−visible absorbance of ZnO. The inset shows the structure of $Zn_{12}O_{12}$. (b) DOS plot of ZnO. (c) LUMO (top) and HOMO (bottom) of the optimized geometrical structure of ZnO. The energy gap between HOMO and LUMO is 3.48 eV. (d) Theoretical UV−visible absorbance of Au−ZnO. The inset shows the structure of Au-doped $Zn_{12}O_{12}$. (e) DOS plot of Au−ZnO. (f) LUMO (top) and HOMO (bottom) of the optimized geometrical structure of Au−ZnO. The energy gap between HOMO and LUMO is 1.89 eV.
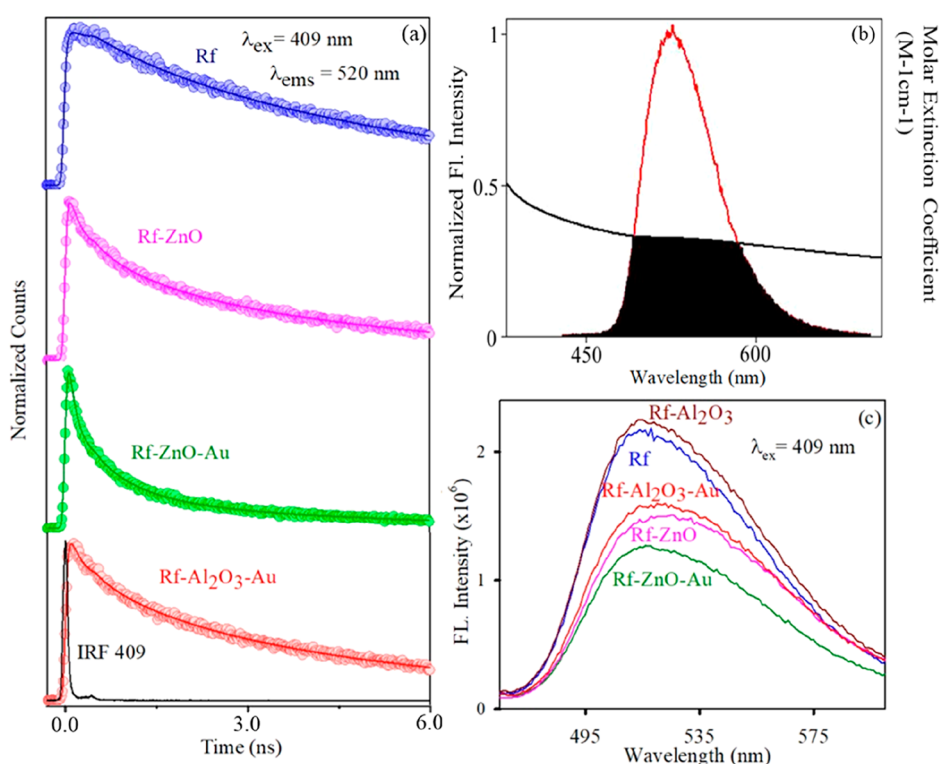

Figure 4. (a) Picosecond-resolved fluorescence transients of Rf (blue), Rf−ZnO (pink), Rf−ZnO−Au (green), and Rf−Al$_2$O$_3$−Au (red) in ethanol. (b) Spectral overlap between emission of Rf (red) and absorption of Au−ZnO (black). (c) Room-temperature emission spectra of Rf (blue), Rf−ZnO (pink), Rf−ZnO−Au (green), Rf−Al$_2$O$_3$ (gray), and Rf−Al$_2$O$_3$−Au (red) in ethanol.

(CB) of Rf, which are separated by an energy gap of 2.7 eV. Figure S4b shows the electron delocalization of Rf at the HOMO and LUMO.

The structure of pristine $Zn_{12}O_{12}$ is prepared by eight hexagons of (ZnO)$_3$ and six tetragons of (ZnO)$_2$ rings with tetrahedral rotational as well as inversion symmetry. The inset

of Figure 3a depicts the structural geometry of pristine $Zn_{12}O_{12}$. The average bond lengths of hexagons (L1) and tetragons (L2) are about 1.88 and 1.96 Å, respectively. The angles in hexagons ($\theta 1$, $\theta 2$) and tetragons ($\theta 3$, $\theta 4$) are 126.68, 112.29, 91.07, and 87.75°, respectively. Recently, the optimized structure of $Zn_{12}O_{12}$ using DFT/B3LYP exchange

Table 1. Lifetime of Picosecond Time-Resolved Fluorescence Transients of Rf, Rf—ZnO, Rf—ZnO—Au, and Rf—Al$_2$O$_3$—Au in Ethanol

system	excitation wavelength (nm)	emission wavelength (nm)	τ_1 (ps)	τ_2 (ps)	τ_2 (ps)	τ_{avg} (ps)
Rf	409	520	643 (33.20%)	5313 (66.80%)		3762.56
Rf—ZnO	409	520	54 (46.33%)	646 (28.67%)	5020 (25%)	1466.23
Rf—ZnO—Au	409	520	48 (54.6%)	155 (32.3%)	4202 (13.1%)	626.84
Rf—Al$_2$O3—Au	409	520	143 (38.6%)	823 (28.6%)	5098 (32.8%)	1962.72

correlation functions showed that the distances L1 and L2 were 1.85 and 1.93 Å, respectively. The calculated $\theta 1$, $\theta 2$, $\theta 3$, and $\theta 4$ angles were obtained to be 126.41, 112.37, 91.97, and 86.92°, respectively.[41] It can be concluded that the obtained theoretical results well matches with previously reported literature values.[41,42] The absorption spectrum of Zn$_{12}$O$_{12}$ is calculated by using the same exchange correlation function. The calculated absorption peak is found to be at a wavelength of 350 nm, as shown in Figure 4a, which is well consistent with our experimental absorption spectra.[35] The TDOS of Zn$_{12}$O$_{12}$ is calculated using the B3LYP exchange correlation functional method and plotted in GaussSum 2.1.4 software, as shown in Figure 3b. It depicts proper orbital delocalization in VB and CBs of Zn$_{12}$O$_{12}$ NPs. The HOMO and LUMO of Zn$_{12}$O$_{12}$ are separated by a band gap of 3.48 eV, which well matches with the reported literature.[34] Figure 3c depicts surfaces of the frontier molecular orbitals (HOMO/LUMO) of Zn$_{12}$O$_{12}$. The molecular orbitals (HOMO and LUMO) of the Zn$_{12}$O$_{12}$ NPs are localized on the respective Zn and O sites, which imply that the Zn sites are electrophilic and O sites are nucleophilic in nature. The Au-doped Zn$_{12}$O$_{12}$ NPs are prepared by replacing two Zn atoms of the optimized Zn$_{12}$O$_{12}$ structure with two Au atoms. The inset of Figure 3d depicts the optimized geometry of the Au-doped Zn$_{12}$O$_{12}$ structure calculated by the B3LYP/6-311++G (d,p)-SDD-based method. The UV—vis absorption spectra of Au-doped Zn$_{12}$O$_{12}$ are calculated with the most stable geometry of hybrids, as shown in Figure 3d, which well matches with our experimental results. The TDOS of Au-doped Zn$_{12}$O$_{12}$ NPs is calculated, as shown in Figure 3e. The doping of Au shifts the HOMO level to higher energies and consequently the band gap becomes comparatively narrowed. The calculated band gap is found to be 1.89 eV, which indicates the formation of Au-doped Zn$_{12}$O$_{12}$ hybrid nanomaterials. The surfaces of the frontier molecular orbitals (HOMO/LUMO) of the Au-doped Zn$_{12}$O$_{12}$ hybrid are depicted in Figure 3f. It depicts the electron density being shifted toward Au due to a higher electron affinity. The attachment of Rf on the surface of Au—ZnO is optimized by using the DFT/B3LYP method, as shown in Figure S5a. The DOS of Rf—ZnO—Au (Figure S5b) depicts some additional states, which indicates the electron transfer process from the LUMO of Rf to the CB of ZnO.[43]

In order to study the charge-transfer process, the pico-second-resolved fluorescence experiment is performed. The time-resolved transients depict the faster fluorescence decay for both Rf—ZnO and Rf—ZnO—Au nanohybrids, as compared to the Rf only solution (Figure 4a). The fluorescence decay was monitored at 520 nm with excitation of a 409 nm laser source. The fluorescence transient of Rf is characterized by two time constants of 643 and 5313 ps with an average lifetime of 3762 ps, which decreases significantly for Rf—ZnO due to the presence of an additional faster component of ~54 ps (having 46.33% contribution). The faster component of 54 ps is attributed to the interfacial excited-state photoelectron-transfer

process from the LUMO of Rf to the CB of ZnO NPs.[44−46] In the case of the Rf—ZnO—Au nanohybrid, the faster component of 48 ps is attributed to interfacial excited-state electron transfer.[15] It has to be stated that the time component of 155 ps could be manifestation of FRET from Rf to Au.[44] Moreover, we have introduced the Rf—Al$_2$O$_3$—Au nanohybrid (Al$_2$O$_3$ is an insulator) and measured time-resolved fluorescence for further clarification. Herein, the time constant of 143 ps (contribution of 38.6%) indicates the energy transfer from Rf to Au NPs (since Al$_2$O$_3$ is an insulator, the possibility of the excited-state photoelectron-transfer process from Rf to Al$_2$O$_3$ is insignificant). In the case of the Rf—ZnO—Au nanohybrid, almost a similar time constant of 155 ps implies the energy transfer from Rf to Au. The fitting parameters of fluorescence transient are listed in Table 1. Moreover, the overlap between the emission of the donor (Rf) and the absorption of the acceptor, as shown in Figure 4b (herein, gold is the acceptor), confirms the possibility of significant dipolar coupling between Rf and Au. The steady-state emission of all the samples is represented in Figure 4c. It shows significant emission quenching of Rf—Al$_2$O$_3$—Au with respect to only Rf, which also indicates the FRET between RF and Au. The scheme of FRET is created to determine the distance between the donor and the acceptor using eq 2. The FRET efficiency and the overlap integral $[J(\lambda)]$ are calculated to be 47.83% and 5.89 × 10^{15} M^{-1} cm^{-1} nm^4, respectively. The distance between the donor (Rf) and the acceptor (surface of Au NPs) is found to be 5.11 ± 0.025 nm, which is within the probing limit of FRET (1−10 nm). The presence of Au NPs with the SPR band influences the enhanced electron injection from Au to ZnO, as evident from other reported literature studies.[47−50]

Photoinduced ROS generation is illustrated using a well-known non-fluorescent marker, DCFH. DCFH oxidizes to fluorescent dichlorofluorescein (DCF) by ROS, exhibiting an emission near 520 nm upon excitation at 488 nm. Thus, the enhancement of the ROS level is demonstrated by the enhancement of the emission intensity at 520 nm.[51] The oxidation of DCFH is monitored for 8 min in the dark and then under irradiation of blue light for 24 min. In the dark, there is no enhancement of emission intensity at 520 nm. However, with the increase in the light exposure time, a greater enhancement of emission intensity is observed for the Rf—Au—ZnO nanohybrid as compared to Rf—ZnO, Rf—Al$_2$O$_3$—Au, Rf, and others as controls (Figure 5a). On the other hand, Rf—ZnO produces greater ROS as compared to Rf—Al$_2$O$_3$—Au, Rf—Al$_2$O$_3$, Au—ZnO, Rf, and DCFH only. In the course of the excited-state photoelectron-transfer process of the Rf—ZnO nanohybrid, the separated free electrons and the holes produce a significant amount of ROS (free electrons produce superoxide from oxygen molecules, and holes generate hydroxyl radicals from water molecules) from neighboring oxygen and water molecules.[52−54] In the case of the Rf—ZnO—Au nanohybrid, the energy transfer from Rf to Au NPs takes place due to dipolar coupling between Rf and Au NPs. Besides
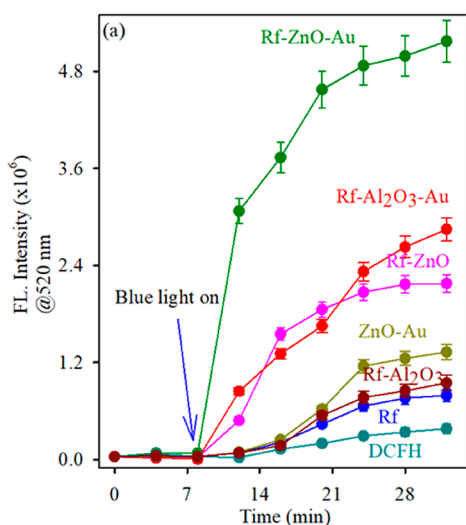
Figure 5. (a) DCFH oxidation (monitored at 520 nm) with time in the presence of Rf (blue), Rf−ZnO (pink), Rf−ZnO−Au (green), Rf−Al$_2$O$_3$ (gray), Rf−Al$_2$O$_3$−Au (red), and DCFH (cyan) only under the dark (8 min) and blue light (24 min).
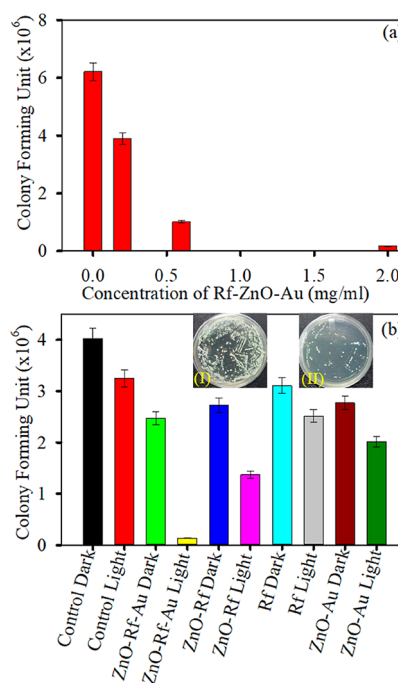

Figure 6. (a) Dose-dependent antibacterial effect of Rf−ZnO−Au at concentrations ranging from 0 to 2 mg/mL on MRSA under dark conditions. (b) Bacterial viability after treatment with 0.2 mg/mL Rf−ZnO−Au in the presence and absence of blue-light irradiation (30 min). The inset shows images of MRSA plates treated with Rf−ZnO−Au before (I) and after (II) blue-light irradiation.

the photoelectron transfer process from the excited state of Rf to the CB of ZnO in the Rf−ZnO−Au nanohybrid, the dipolar coupling between Rf and Au NPs also leads to electron transfer from Au NPs to the CB of ZnO.[48−50] There seems to be a huge charge separation in the Rf−ZnO−Au nanohybrid upon excitation, which results in an excessive amount of ROS production over the Rf−ZnO nanohybrid and other controls under blue-light irradiation.

Next, we have evaluated the antimicrobial action of Rf−ZnO and Rf−Au−ZnO toward MRSA in the dark and under blue-light illumination. In order to determine the dose-dependent toxicity of the RF−ZnO−Au nanohybrid toward MRSA, the variable concentration of Rf−ZnO−Au (ranging from 0 to 2 mg/mL) was examined on the growth of MRSA using the cfu assay under dark conditions (Figure 6a). The minimum inhibition in the bacterial growth was observed at a concentration of 0.2 mg/mL, whereas at a concentration of 1 mg/mL, the inhibition of bacterial growth is quite significant. In order to examine the photodynamic action, a concentration of 0.2 mg/mL of the Rf−ZnO−Au nanohybrid has been prepared. Next, the concentration of 0.2 mg/mL was kept under incubation with the culture of MRSA for 3 h in the dark prior to 30 min irradiation of blue light. The inset of Figure 6b shows the pictures of MRSA culture plates treated with the Rf−ZnO−Au nanohybrid in the absence and in the presence of blue-light illumination. The images of MRSA plates show that the bacterial CFU are significantly less in number in the presence of light as compared to those in the dark. There is no antibacterial activity observed under dark and light-irradiated conditions for the control-treated samples (Figure 6b). In the case of the Rf−ZnO-treated sample, the bacterial growth is observed to have decreased by 65.9% in CFU compared to 96.7% for the Rf−ZnO−Au nanohybrid-treated samples under irradiation with blue light. Thus, the inhibition in the growth of bacteria for the Rf−ZnO−Au nanohybrid is the highest (96.7%) relative to the other controls.

5. CONCLUSIONS

We have explored the effectiveness of the Rf−ZnO−Au nanohybrid in visible light harvesting over the Rf−ZnO

nanohybrid for implementation in PDT. The attachment of Rf on the ZnO surface and the Au−ZnO surface was characterized by electron microscopy, optical spectroscopy, and DFT analysis techniques. The DFT- and TD-DFT-based calculations corroborate the results from the experimental data. The picosecond-resolved fluorescence transient shows the excited-state electron-transfer dynamics of Rf−ZnO and Rf−ZnO−Au. The photoinduced excited-state charge transfer from Rf to ZnO in the nanohybrid is responsible for overall efficient ROS generation over the free Rf dye. Besides the excited-state photoelectron-transfer process, the presence of Au on the ZnO surface influences the dipolar coupling between Au and Rf, which leads to a huge charge separation in the Rf−ZnO−Au nanohybrid upon excitation at blue light. This huge charge separation upon excitation results in greater production of ROS for the Rf−ZnO−Au nanohybrid over the Rf−ZnO nanohybrid. The key advantage of Au on the ZnO surface in the Rf−ZnO−Au nanohybrid is the enhancement of efficiency in ROS generation. The photodynamic antibacterial action on MRSA by both Rf−ZnO and Rf−ZnO−Au nanohybrids is confirmed by the cfu assay. After incubation of MRSA with the Rf−ZnO−Au nanohybrid, a significant reduction (96.7%) in cfu's was observed upon blue-light irradiation. Overall, the results highlight the crucial role of the plasmonic NPs in the Rf−ZnO−Au nanohybrid which influences the efficiency of ROS production and hence antibacterial activity under blue-light irradiation. It provides a promising aspect for the improvement of visible-/NIR-light driven PDT, which could be translated for other suitable photosensitizers.

■ ASSOCIATED CONTENT

ⓢ Supporting Information

The Supporting Information is available free of charge at https://pubs.acs.org/doi/10.1021/acsphyschemau.1c00033.

Low-magnification TEM images of Au−ZnO; EDAX spectra of Au−ZnO; theoretical UV−visible absorbance and emission spectra of Rf; DOS plot of Rf; HOMO and LUMO of the optimized geometrical structure of Rf; attachment of Rf on the surface of Au−ZnO; DOS plot of Rf−ZnO−Au; and compositional analysis of the Au−ZnO nanohybrid collected from EDAX (PDF)

■ AUTHOR INFORMATION

Corresponding Author

Samir Kumar Pal − *Department of Chemical, Biological & Macromolecular Sciences, S. N. Bose National Centre for Basic Sciences, Kolkata 700106, India;* ⓞ orcid.org/0000-0001-6943-5828; Email: skpal@bose.res.in

Authors

Arpan Bera − *Department of Chemical, Biological & Macromolecular Sciences, S. N. Bose National Centre for Basic Sciences, Kolkata 700106, India*

Md. Nur Hasan − *Department of Chemical, Biological & Macromolecular Sciences, S. N. Bose National Centre for Basic Sciences, Kolkata 700106, India;* ⓞ orcid.org/0000-0001-7826-5613

Arka Chatterjee − *Department of Chemical, Biological & Macromolecular Sciences, S. N. Bose National Centre for Basic Sciences, Kolkata 700106, India*

Dipanjan Mukherjee − *Department of Chemical, Biological & Macromolecular Sciences, S. N. Bose National Centre for Basic Sciences, Kolkata 700106, India*

Complete contact information is available at:
https://pubs.acs.org/10.1021/acsphyschemau.1c00033

Notes

The authors declare no competing financial interest.

■ ACKNOWLEDGMENTS

■ REFERENCES

(1) Brodin, N. P.; Guha, C.; Tomé, W. A. Photodynamic therapy and its role in combined modality anticancer treatment. *Technol. Cancer Res. Treat.* **2015**, *14*, 355−368.

(2) Li, Y.; Lv, S.; Song, Z.; Dang, J.; Li, X.; He, H.; Xu, X.; Zhou, Z.; Yin, L. Photodynamic therapy-mediated remote control of chemotherapy toward synergistic anticancer treatment. *Nanoscale* **2018**, *10*, 14554−14562.

(3) Zhang, J.; Jiang, C.; Figueiró Longo, J. P.; Azevedo, R. B.; Zhang, H.; Muehlmann, L. A. An updated overview on the development of new photosensitizers for anticancer photodynamic therapy. *Acta Pharm. Sin. B* **2018**, *8*, 137−146.

(4) Hasan, M. N.; Bera, A.; Maji, T. K.; Pal, S. K. Sensitization of nontoxic MOF for their potential drug delivery application against microbial infection. *Inorg. Chim. Acta* **2021**, *523*, 120381.

(5) Cardoso, D. R.; Libardi, S. H.; Skibsted, L. H. Riboflavin as a photosensitizer. Effects on human health and food quality. *Food Funct.* **2012**, *3*, 487−502.

(6) Huang, R.; Choe, E.; Min, D. Kinetics for singlet oxygen formation by riboflavin photosensitization and the reaction between riboflavin and singlet oxygen. *J. Food Sci.* **2004**, *69*, C726−C732.

(7) de La Rochette, A.; Silva, E.; Birlouez-Aragon, I.; Mancini, M.; Edwards, A.-M.; Morlière, P. Riboflavin Photodegradation and Photosensitizing Effects are Highly Dependent on Oxygen and Ascorbate Concentrations. *Photochem. Photobiol.* **2000**, *72*, 815−820.

(8) Barton-Wright, E. C.; Moran, T.; Sarson, H. S. Riboflavin and Vitamin B1 in Nineteenth Century Buns and Ale. *Nature* **1943**, *152*, 273.

(9) Huang, R.; Kim, H. J.; Min, D. B. Photosensitizing effect of riboflavin, lumiflavin, and lumichrome on the generation of volatiles in soy milk. *J. Agric. Food Chem.* **2006**, *54*, 2359−2364.

(10) Chaudhuri, S.; Batabyal, S.; Polley, N.; Pal, S. K. Vitamin B2 in nanoscopic environments under visible light: photosensitized antioxidant or phototoxic drug? *J. Phys. Chem. A* **2014**, *118*, 3934−3943.

(11) Zhang, L.; Gu, F.; Chan, J.; Wang, A.; Langer, R.; Farokhzad, O. Nanoparticles in medicine: therapeutic applications and developments. *Clin. Pharmacol. Ther.* **2008**, *83*, 761−769.

(12) Davis, M. E.; Chen, Z.; Shin, D. M. Nanoparticle therapeutics: an emerging treatment modality for cancer. *Nat. Rev. Drug Discov.* **2008**, *7*, 771−782.

(13) Mishra, B.; Patel, B. B.; Tiwari, S. Colloidal nanocarriers: a review on formulation technology, types and applications toward targeted drug delivery. *Nanomedicine* **2010**, *6*, 9−24.

(14) Narvekar, M.; Xue, H. Y.; Eoh, J. Y.; Wong, H. L. Nanocarrier for Poorly Water-Soluble Anticancer Drugs-Barriers of Translation and Solutions. *AAPS PharmSciTech* **2014**, *15*, 822−833.

(15) Bagchi, D.; Rathnam, V. S. S.; Lemmens, P.; Banerjee, I.; Pal, S. K. NIR-Light-active ZnO-based nanohybrids for bacterial biofilm treatment. *ACS Omega* **2018**, *3*, 10877−10885.

(16) Zhao, N.; Yan, L.; Zhao, X.; Chen, X.; Li, A.; Zheng, D.; Zhou, X.; Dai, X.; Xu, F.-J. Versatile types of organic/inorganic nanohybrids: from strategic design to biomedical applications. *Chem. Rev.* **2018**, *119*, 1666−1762.

(17) Tan, L. L.; Shang, L. Smart Delivery Systems Based on Poly(glycidyl methacrylate)s-Coated Organic/Inorganic Core-Shell Nanohybrids. *Macromol. Rapid Commun.* **2019**, *40*, 1800879.

(18) Liang, C.; Zhang, X.; Wang, Z.; Wang, W.; Yang, M.; Dong, X. Organic/inorganic nanohybrids rejuvenate photodynamic cancer therapy. *J. Mater. Chem. B* **2020**, *8*, 4748−4763.

(19) Huang, X.; Zheng, X.; Xu, Z.; Yi, C. ZnO-based nanocarriers for drug delivery application: From passive to smart strategies. *Int. J. Pharm.* **2017**, *534*, 190−194.

(20) Siegers, C.; Hohl-Ebinger, J.; Zimmermann, B.; Würfel, U.; Mülhaupt, R.; Hinsch, A.; Haag, R. A Dyadic Sensitizer for Dye Solar Cells with High Energy-Transfer Efficiency in the Device. *ChemPhysChem* **2007**, *8*, 1548−1556.

(21) Patwari, J.; Sardar, S.; Liu, B.; Lemmens, P.; Pal, S. K. Three-in-one approach towards efficient organic dye-sensitized solar cells: aggregation suppression, panchromatic absorption and resonance energy transfer. *Beilstein J. Nanotechnol.* **2017**, *8*, 1705−1713.

(22) Lee, E.; Kim, C.; Jang, J. High-Performance Förster Resonance Energy Transfer (FRET)-Based Dye-Sensitized Solar Cells: Rational Design of Quantum Dots for Wide Solar-Spectrum Utilization. *Chem. Eur. J.* **2013**, *19*, 10280−10286.

(23) Sarkar, S.; Makhal, A.; Lakshman, K.; Bora, T.; Dutta, J.; Pal, S. K. Dual-sensitization via electron and energy harvesting in CdTe quantum dots decorated ZnO nanorod-based dye-sensitized solar cells. *J. Phys. Chem. C* **2012**, *116*, 14248−14256.

(24) Pandey, A. K.; Ahmad, M. S.; Alizadeh, M.; Rahim, N. A. Improved electron density through hetero-junction binary sensitized

TiO$_2$/CdTe/D719 system as photoanode for dye sensitized solar cell. *Phys. E* **2018**, *101*, 139−143.

(25) Ambapuram, M.; Ramireddy, R.; Maddala, G.; Godugunuru, S.; Yerva, P. V. S.; Mitty, R. Effective Upconverter and Light Scattering Dual Function LiYF$_4$:Er^{3+}/Yb^{3+} Assisted Photoelectrode for High Performance Cosensitized Dye Sensitized Solar Cells. *ACS Appl. Electron. Mater.* **2020**, *2*, 962−970.

(26) Gu, H.; Wang, J.; Li, Y.; Wang, Z.; Fu, Y. The core-shell-structured NaYF$_4$:Er^{3+},Yb^{3+}@NaYF$_4$:Eu^{3+} nanocrystals as dual-mode and multifunctional luminescent mechanism for high-performance dye-sensitized solar cells. *Mater. Res. Bull.* **2018**, *108*, 219−225.

(27) Craciun, A. M.; Focsan, M.; Magyari, K.; Vulpoi, A.; Pap, Z. Surface Plasmon Resonance or Biocompatibility-Key Properties for Determining the Applicability of Noble Metal Nanoparticles. *Materials* **2017**, *10*, 836.

(28) Chaudhuri, S.; Sardar, S.; Bagchi, D.; Singha, S. S.; Lemmens, P.; Pal, S. K. Sensitization of an endogenous photosensitizer: electronic spectroscopy of riboflavin in the proximity of semiconductor, insulator, and metal nanoparticles. *J. Phys. Chem. A* **2015**, *119*, 4162−4169.

(29) Ahmed, S. A.; Hasan, M. N.; Bagchi, D.; Altass, H. M.; Morad, M.; Jassas, R. S.; Hameed, A. M.; Patwari, J.; Alessa, H.; Alharbi, A.; Pal, S. K. Combating essential metal toxicity: key information from optical spectroscopy. *ACS Omega* **2020**, *5*, 15666−15672.

(30) Hamprecht, F. A.; Cohen, A. J.; Tozer, D. J.; Handy, N. C. Development and assessment of new exchange-correlation functionals. *J. Chem. Phys.* **1998**, *109*, 6264−6271.

(31) Miehlich, B.; Savin, A.; Stoll, H.; Preuss, H. Results obtained with the correlation energy density functionals of becke and Lee, Yang and Parr. *Chem. Phys. Lett.* **1989**, *157*, 200−206.

(32) Vosko, S. H.; Wilk, L.; Nusair, M. Accurate spin-dependent electron liquid correlation energies for local spin density calculations: a critical analysis. *Can. J. Phys.* **1980**, *58*, 1200−1211.

(33) Krishnan, R.; Binkley, J. S.; Seeger, R.; Pople, J. A. Self-consistent molecular orbital methods. XX. A basis set for correlated wave functions. *J. Chem. Phys.* **1980**, *72*, 650−654.

(34) Ammar, H. Y.; Badran, H. M.; Umar, A.; Fouad, H.; Alothman, O. Y. ZnO Nanocrystal-Based Chloroform Detection: Density Functional Theory (DFT) Study. *Coatings* **2019**, *9*, 769.

(35) Hasan, M. N.; Maji, T. K.; Pal, U.; Bera, A.; Bagchi, D.; Halder, A.; Ahmed, S. A.; Al-Fahemi, J. H.; Bawazeer, T. M.; Saha-Dasgupta, T.; Pal, S. K. Wide bandgap semiconductor-based novel nanohybrid for potential antibacterial activity: ultrafast spectroscopy and computational studies. *RSC Adv.* **2020**, *10*, 38890−38899.

(36) Li, L.; Hu, J.; Shi, X.; Ruan, W.; Luo, J.; Wei, X. Theoretical Studies on Structures, Properties and Dominant Debromination Pathways for Selected Polybrominated Diphenyl Ethers. *Int. J. Mol. Sci.* **2016**, *17*, 927.

(37) O'boyle, N. M.; Tenderholt, A. L.; Langner, K. M. cclib: A library for package-independent computational chemistry algorithms. *J. Comput. Chem.* **2008**, *29*, 839−845.

(38) Liu, X.; Atwater, M.; Wang, J.; Huo, Q. Extinction coefficient of gold nanoparticles with different sizes and different capping ligands. *Colloids Surf., B* **2007**, *58*, 3−7.

(39) Kumar, S. S.; Venkateswarlu, P.; Rao, V. R.; Rao, G. N. Synthesis, characterization and optical properties of zinc oxide nanoparticles. *Int. Nano Lett.* **2013**, *3*, 30.

(40) Chatterjee, A.; Kar, P.; Wulferding, D.; Lemmens, P.; Pal, S. K. Flower-like BiOI microspheres decorated with plasmonic gold nanoparticles for dual detoxification of organic and inorganic water pollutants. *ACS Appl. Nano Mater.* **2020**, *3*, 2733−2744.

(41) Afshari, T.; Mohsennia, M. Transition metals doped ZnO nanocluster for ethylene oxide detection: A DFT study. *Main Group Met. Chem.* **2019**, *42*, 113−120.

(42) de Oliveira, O. V.; Pires, J. M.; Neto, A. C.; Divino dos Santos, J. Computational studies of the Ca$_{12}$O$_{12}$, Ti$_{12}$O$_{12}$, Fe$_{12}$O$_{12}$ and Zn$_{12}$O$_{12}$ nanocage clusters. *Chem. Phys. Lett.* **2015**, *634*, 25−28.

(43) Maji, T. K.; Hasan, M. N.; Ghosh, S.; Wulferding, D.; Bhattacharya, C.; Lemmens, P.; Karmakar, D.; Pal, S. K. Development of a magnetic nanohybrid for multifunctional application: From immobile photocatalysis to efficient photoelectrochemical water splitting: A combined experimental and computational study. *J. Photochem. Photobiol., A* **2020**, *397*, 112575.

(44) Patwari, J.; Chatterjee, A.; Sardar, S.; Lemmens, P.; Pal, S. K. Ultrafast dynamics in co-sensitized photocatalysts under visible and NIR light irradiation. *Phys. Chem. Chem. Phys.* **2018**, *20*, 10418−10429.

(45) Chaudhuri, S.; Sardar, S.; Bagchi, D.; Dutta, S.; Debnath, S.; Saha, P.; Lemmens, P.; Pal, S. K. Photoinduced dynamics and toxicity of a cancer drug in proximity of inorganic nanoparticles under visible light. *ChemPhysChem* **2016**, *17*, 270−277.

(46) Koops, S. E.; O'Regan, B. C.; Barnes, P. R. F.; Durrant, J. R. Parameters influencing the efficiency of electron injection in dye-sensitized solar cells. *J. Am. Chem. Soc.* **2009**, *131*, 4808−4818.

(47) Reineck, P.; Gómez, D.; Ng, S. H.; Karg, M.; Bell, T.; Mulvaney, P.; Bach, U. Distance and Wavelength Dependent Quenching of Molecular Fluorescence by Au@SiO$_2$ Core-Shell Nanoparticles. *ACS Nano* **2013**, *7*, 6636−6648.

(48) Erwin, W. R.; Zarick, H. F.; Talbert, E. M.; Bardhan, R. Light trapping in mesoporous solar cells with plasmonic nanostructures. *Energy Environ. Sci.* **2016**, *9*, 1577−1601.

(49) Kochuveedu, S. T.; Son, T.; Lee, Y.; Lee, M.; Kim, D.; Kim, D. H. Revolutionizing the FRET-based light emission in core-shell nanostructures via comprehensive activity of surface plasmons. *Sci. Rep.* **2014**, *4*, 4735.

(50) Kang, K. A.; Wang, J.; Jasinski, J. B.; Achilefu, S. Fluorescence manipulation by gold nanoparticles: from complete quenching to extensive enhancement. *J. Nanobiotechnol.* **2011**, *9*, 16.

(51) Ahmed, S. A.; Hasan, M. N.; Bagchi, D.; Altass, H. M.; Morad, M.; Althagafi, I. I.; Hameed, A. M.; Sayqal, A.; Khder, A. E. R. S.; Asghar, B. H.; Katouah, H. A.; Pal, S. K. Nano-MOFs as targeted drug delivery agents to combat antibiotic-resistant bacterial infections. *R. Soc. Open Sci.* **2020**, *7*, 200959.

(52) He, W.; Kim, H.-K.; Wamer, W. G.; Melka, D.; Callahan, J. H.; Yin, J.-J. Photogenerated charge carriers and reactive oxygen species in ZnO/Au hybrid nanostructures with enhanced photocatalytic and antibacterial activity. *J. Am. Chem. Soc.* **2014**, *136*, 750−757.

(53) He, W.; Wu, H.; Wamer, W. G.; Kim, H.-K.; Zheng, J.; Jia, H.; Zheng, Z.; Yin, J.-J. Unraveling the enhanced photocatalytic activity and phototoxicity of ZnO/metal hybrid nanostructures from generation of reactive oxygen species and charge carriers. *ACS Appl. Mater. Interfaces* **2014**, *6*, 15527−15535.

(54) Kang, Z.; Yan, X.; Zhao, L.; Liao, Q.; Zhao, K.; Du, H.; Zhang, X.; Zhang, X.; Zhang, Y. Gold nanoparticle/ZnO nanorod hybrids for enhanced reactive oxygen species generation and photodynamic therapy. *Nano Res.* **2015**, *8*, 2004−2014.